# High-angular-momentum structures in $^{64}$Zn

D. Karlgren,[1,2] R. M. Clark,[1] I. Ragnarsson,[1,3] C. E. Svensson,[1,*] D. Ward,[1] R. Wyss,[2] C. Andreoiu,[4,†] R. A. E. Austin,[5] M. P. Carpenter,[6] M. Cromaz,[1] M. A. Deleplanque,[1] R. M. Diamond,[1] P. Fallon,[1] A. Görgen,[1,‡] R. V. F. Janssens,[6] T. L. Khoo,[6] F. Kondev,[6,§] G. J. Lane,[1,‖] T. Lauritsen,[6] I. Y. Lee,[1] A. O. Macchiavelli,[1] T. Rodinger,[5] D. Rudolph,[4] D. G. Sarantites,[7] D. Seweryniak,[6] T. Steinhardt,[8] F. S. Stephens,[1] O. Thelen,[8] K. Vetter,[1,¶] and J. C. Waddington[5]

[1]*Nuclear Science Division, Lawrence Berkeley National Laboratory, Berkeley, California 94720, USA*

[2]*KTH, Royal Institute of Technology, Frescativägen 24, S-10405 Stockholm, Sweden*

[3]*Division of Mathematical Physics, Lund Institute of Technology, S-22100 Lund, Sweden*

[4]*Department of Physics, Lund University, S-22100 Lund, Sweden*

[5]*Department of Physics and Astronomy, McMaster University, Hamilton, Ontario, Canada L8S 4M1*

[6]*Physics Division, Argonne National Laboratory, Argonne, Illinois 60439, USA*

[7]*Chemistry Department, Washington University, St. Louis, Missouri 63130, USA*

[8]*Institut für Kernphysik, Universität zu Köln, D-50937 Köln, Germany*

(Received 6 June 2003; published 25 March 2004)

High-angular-momentum states in $^{64}$Zn were populated in the $^{40}$Ca($^{28}$Si,$4p$) reaction at a beam energy of 122 MeV. Evaporated, light, charged particles were identified by the Microball, while $\gamma$ rays were detected using the Gammasphere array. The main focus of this paper is on two strongly coupled, collective bands. The yrast band, which was previously known, has been linked to lower-lying states establishing the excitation energies and angular momenta of in-band states for the first time. The newly identified excited band decays to the yrast band but firm angular-momentum assignments could not be made. In order to interpret these structures cranked-Nilsson-Strutinsky calculations have been performed. The calculations have been extended to account for the distribution of nucleons within a configuration. The yrast collective band is interpreted as based on the $\pi(f_{7/2})^{-1}(p_{3/2}f_{5/2})^2(g_{9/2})^1\nu(p_{3/2}f_{5/2})^4(g_{9/2})^2$ configuration. There are several possible interpretations of the second band but it is difficult to distinguish between the different possibilities.

DOI: 10.1103/PhysRevC.69.034330 PACS number(s): 21.10.Re, 23.20.Lv, 27.50.+e

## I. INTRODUCTION

Recent observations of rotational bands in the proton-rich nuclei near $A \simeq 60$ are of considerable current interest [1–13]. The limited number of valence particles outside of the spherical doubly magic nucleus $^{56}$Ni means that the low-angular-momentum decay schemes are dominated by spherical shell-model states. At higher angular momentum, collective bands dominate. Such bands provide an important testing ground for nuclear models enabling comparisons to be made between mean-field cranking models, traditionally used to describe collective behavior in heavier nuclei, and large-scale shell-model calculations.

The first rotational structure identified in this region was a strongly coupled band assigned to $^{64}$Zn [2]. The characteristics of this band were very similar to those of smoothly terminating rotational bands in the Sn-Sb nuclei of the $A \simeq 110$ region [14]. Such terminating bands are expected in the $A \simeq 60$ region since the maximum angular momentum available from possible configurations is often limited to $I \simeq 20-30\,\hbar$. Comparisons of the $^{64}$Zn structure with cranked-Nilsson-Strutinsky (CNS) calculations suggested a single-particle configuration involving a proton excitation across the $Z=28$ spherical shell gap from the $f_{7/2}$ to the $g_{9/2}$ subshells, coupled with the excitation of two of the valence neutrons into the $g_{9/2}$ subshell. However, in the previous work of Ref. [2] no transitions linking the band to lower-lying yrast states were observed and angular momentum and parity assignments were not possible. Motivated by the above considerations an experiment has been performed to investigate collective structures in $^{64}$Zn.

## II. EXPERIMENTAL DETAILS

### A. Analysis

High-angular-momentum states were populated in the $^{40}$Ca($^{28}$Si,$4p$) reaction at a beam energy of 122 MeV. The beam, accelerated by the ATLAS accelerator at the Argonne National Laboratory, was incident on a $\simeq$400 $\mu$g/cm$^2$ $^{40}$Ca foil with a flash of $\simeq$100 $\mu$g/cm$^2$ Au on both sides to prevent oxidation. $\gamma$ rays were detected with the Gammasphere array [15] which, for this experiment, comprised 101 HPGe detectors. Light charged particles were detected with the Mi-

*Present address: Department of Physics, University of Guelph, Guelph, Ontario, Canada NIG 2W1.

†Present address: Oliver Lodge Laboratory, University of Liverpool, Liverpool L69 7ZE, United Kingdom.

‡Present address: DAPNIA/SPhN, CEA Saclay, F–91191 Gif–sur–Yvette, France.

§Present address: Technology Development Division, Argonne National Laboratory, Argonne, IL 60439.

‖Present address: Department of Nuclear Physics, The Australian National University, Canberra ACT 0200, Australia.

¶Present address: Glenn T. Seaborg Institute, Lawrence Livermore National Laboratory, Livermore, CA 94550.

 

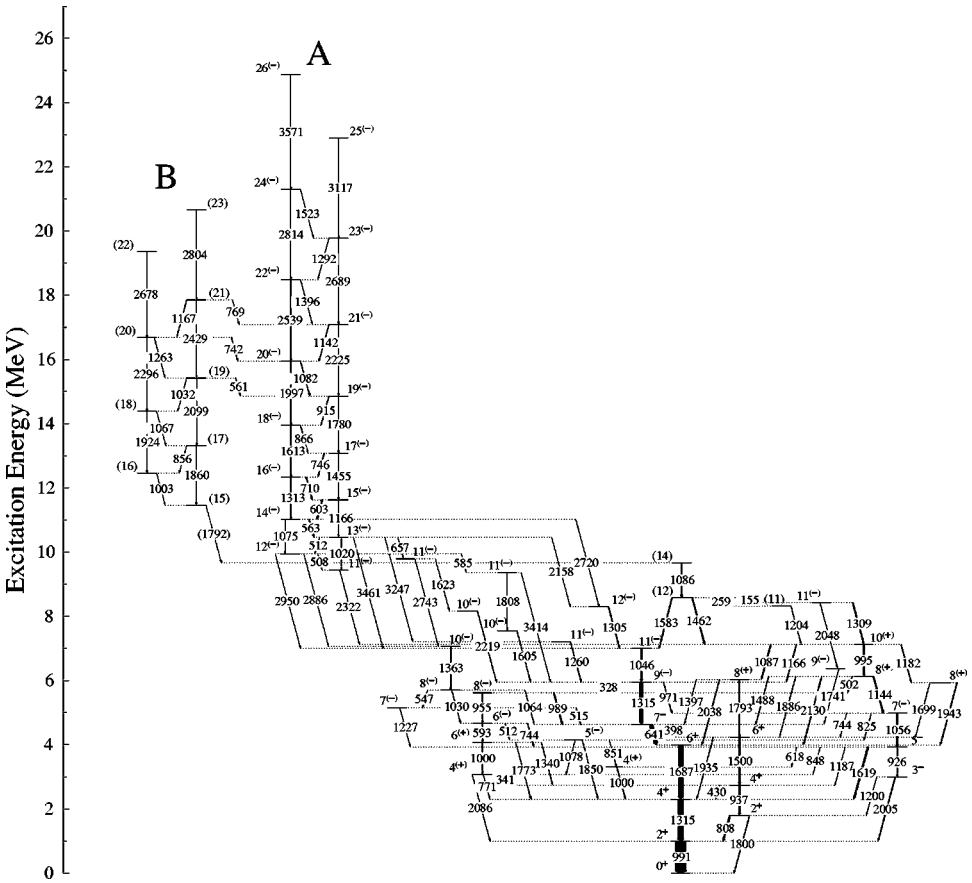


FIG. 1. Level scheme for $^{64}$Zn from the present experiment. The widths of the arrows are proportional to the measured $\gamma$-ray intensity.

croball [16], a $4\pi$ array of 95 CsI(Tl) scintillators. Hevimet collimators were removed from the BGO suppressors to enable $\gamma$-ray sum-energy and multiplicity measurements [17]. A total of $2.3\times10^9$ coincidence events, with at least four Compton-suppressed $\gamma$ rays, were collected. The $^{64}$Zn residue was produced in approximately 15% of all fusion-evaporation events.

In the analysis, events associated with $^{64}$Zn were selected by requiring the detection of four protons in the Microball (the detection efficiency for a single proton was measured to be 78%) in combination with a requirement that the total energy of the detected protons plus the total $\gamma$-ray energy, measured in Gammasphere, was consistent with that expected for the $4p$ evaporation channel. This latter condition is an application of conservation of total energy and helps to reduce contaminants associated with other reaction channels when one or more of the evaporated particles goes undetected [18]. Over 95% of the fusion-evaporation events passing these requirements were associated with $^{64}$Zn. Contaminant $\gamma$ rays that were positively identified came from the $4pn$, $5p$, and $\alpha 3p$ channels and all had $\simeq$1% intensity relative to the $4p$ channel after the filters. The selected events were then sorted into various $E_\gamma$-$E_\gamma$ coincidence matrices, and $E_\gamma$-$E_\gamma$-$E_\gamma$ cubes. The analysis was performed using the RADWARE suite of programs [19].

During the off-line sorting, a correction to the mean recoil velocity according to the momentum vectors of the detected protons was applied to the $\gamma$ rays on an event-by-event basis [20]. A mean recoil velocity of $v/c=0.0358$ (where $c$ is the speed of light) was used when investigating the low-angular-momentum states. This velocity is appropriate for nuclear states with lifetimes longer than the transit time in the target and was estimated from the mean Doppler shift of $\gamma$-ray transitions, which were emitted after the nucleus recoiled into vacuum. For high-angular-momentum states a mean recoil velocity of $v/c=0.0397$ was used and is more appropriate for states which have lifetimes that are much shorter than the transit time through the target. This corresponds to the calculated recoil velocity for nuclei formed at mid-target and improves the energy resolution of $\gamma$ rays emitted from states in collective bands. These two corrections are referred to as "slow" and "fast," respectively.

### B. Results

#### *1. The level scheme*

The level scheme established by previous works [2,21–24] has been considerably modified and extended. A partial level scheme derived from the experiment is presented in Fig. 1. The main focus of this paper is on the two strongly coupled bands labeled *A* and *B*. As an illustration of the quality of the data, Fig. 2 shows a spectrum associated with a single coincidence gate on the 2689 keV transition in band *A*. This strongly coupled band is the previously known collective band [2] and it collects approximately 10% of the intensity of the $2^+\rightarrow0^+$, 991 keV ground-state transition. The topmost states have been extended by the addition of the 2814, 3571, and 3117 keV transitions. The 3461 keV transition was placed at the top of the band in the previous work

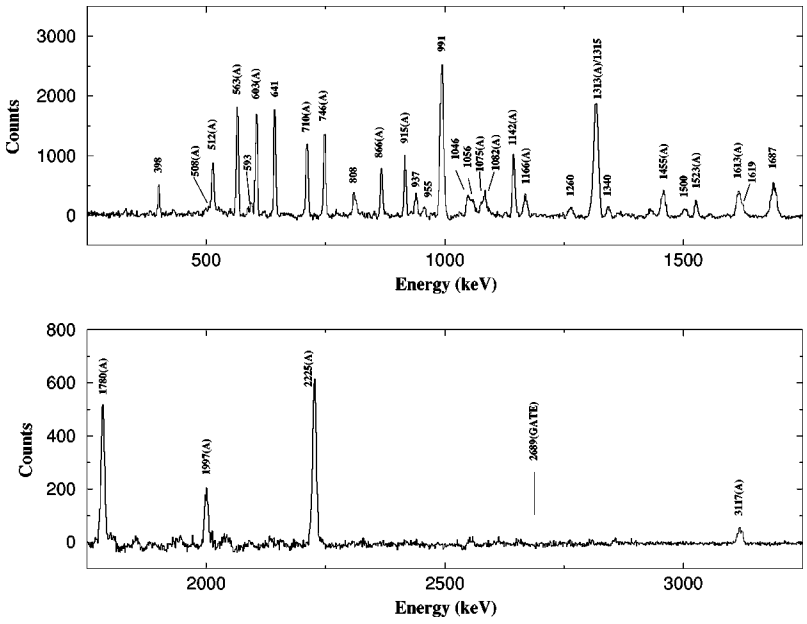


FIG. 2. Low and high energy portions (top and bottom, respectively) of a coincidence spectrum obtained from the "fast" matrix by requiring a single gate on the 2689 keV transition of band *A*. In-band transitions are labeled "A."

[2] and has been reassigned as a transition decaying from near the bottom of the band. The band has also been extended towards lower angular momentum by the addition of the 1020 keV transition. The structure has been firmly linked to low-lying states. Figure 3 shows the high energy portion of the spectrum derived from a single gate on the 603 keV in-band transition in the "slow" matrix. Several of the linking transitions can be clearly seen.

Band *B* is a newly observed structure with an intensity $\simeq$1% relative to the $2^+ \rightarrow 0^+$ 991 keV transition. Figure 4 shows a coincidence spectrum associated with a single gate on the 2429 keV transition in band *B*. It is clear from Fig. 4 that the 2429 keV transition is in coincidence with transitions of band *A* indicating that there is some connection between the two structures. Indeed, as shown in the level scheme of Fig. 1, a number of transitions (561, 742, 769 keV) have been identified which decay from the upper states of band *B* to lower states in band *A*. Each of these interband transitions carries approximately 30% of the total observed decay intensity from their respective initial states. To illustrate the interband decays, Fig. 5 presents a spectrum generated by requiring a double coincidence between the 563 keV transition in band *A* with the 2429 keV transition of band *B*. The 563 keV interband transition is clearly visible as are the expected coincidences with other members of band *A*. Requiring a double coincidence between the 563 keV transition in band *A* with the 2099 keV transition of band *B* shows no connection is present (see Fig. 5). Such coincidence relationships helped with the identification of the interband decay pathways shown in Fig. 1. A 1792 keV $\gamma$ ray has been tentatively placed which decays from the lowest observed in-band state into a lower-lying state.

#### *2. Angular-momentum assignments*

To determine the angular momenta of states, angular correlation (AC) ratios were analyzed. Such an AC ratio was defined by the intensity, corrected for detection efficiency, of a given pair of coincident transitions in the two $E_\gamma$-$E_\gamma$ matrices corresponding to $\pm 35° / \pm 35°$ and $\pm 80° / \pm 80°$, where $\pm 35°$ was formed from summing the subset of detectors with angles (relative to the beam axis) $\theta = \pm 31.7°$ and $\pm 37.4°$, and $\pm 80°$ from the subset with $\theta = \pm 79.2°$ and $\pm 80.7°$. Thus, the AC ratio is defined as

$$R_{AC} = \frac{\mathcal{I}_{\gamma\gamma}(\pm 35, \pm 35)}{\mathcal{I}_{\gamma\gamma}(\pm 80, \pm 80)} \tag{1}$$

Coincident pairs of known stretched *E*2 transitions provided a measure of the nuclear spin alignment given by the dimensionless parameter $\sigma/I$ where, for an initial state of angular momentum *I*, it is assumed that there is a Gaussian distribution of *m* substates centered at $m=0$ with standard

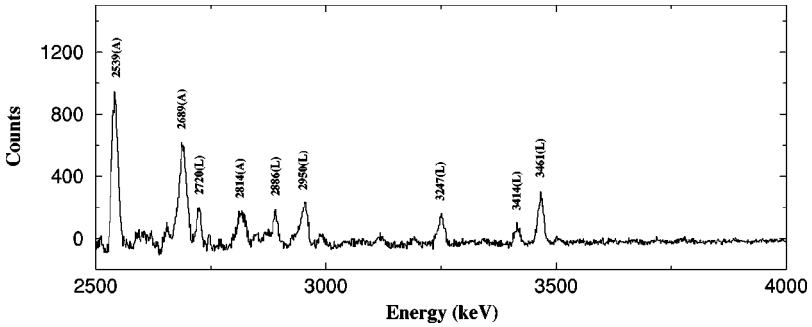


FIG. 3. Coincidence spectrum obtained from the "slow" matrix by requiring a single gate on the 603 keV transition of band *A*. The transitions linking the band to lower lying states are labeled "L" while in-band $\gamma$ rays are labeled "A."

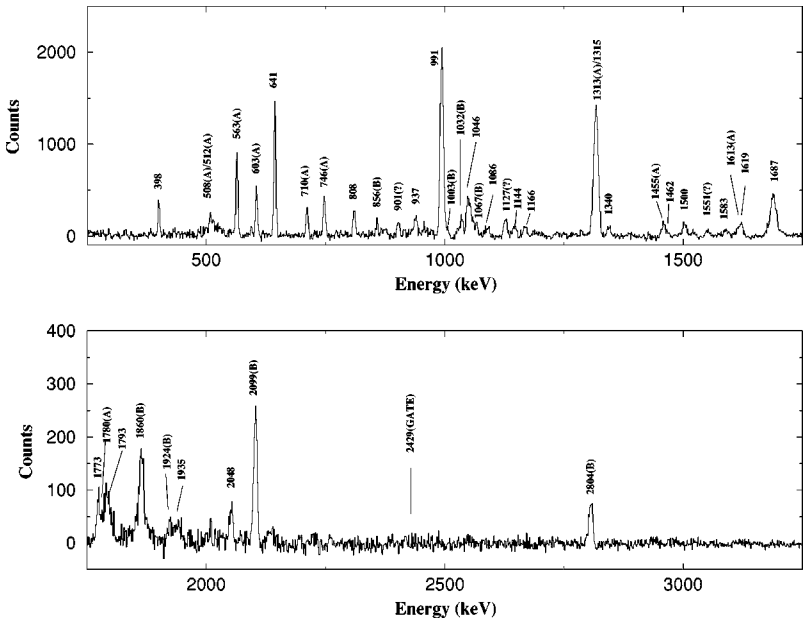


FIG. 4. Low and high energy portions (top and bottom, respectively) of a coincidence spectrum obtained from the "fast" matrix by requiring a single gate on the 2429 keV transition of band *B*. In-band transitions are labeled "B," transitions in band *A* are labeled "A," and coincident transitions not yet placed in the level scheme are labeled "?".

deviation $\sigma$. For such transitions a value of $R_{AC}=1.74(10)$ was measured, corresponding to $\sigma/I=0.32(4)$ at $I=17$ [see Fig. 6(a)]. This value of $\sigma/I$ was used to estimate the expected $R_{AC}$ values for common correlations ($I\rightarrow I-1\rightarrow I-2, I\rightarrow I-1\rightarrow I-3$, etc. ) and to assign the $I$ values shown in Fig. 1.

Additional information on the angular momentum assignments was obtained by measuring $\gamma$-ray angular anisotropy (AA) ratios. Such a ratio was defined by the intensity, corrected for detector efficiency, of a transition detected at ±35° divided by the intensity when detected at ±80°. Clean spectra were obtained by requiring a coincidence with another transition detected in any other detector, regardless of angle. By summing over all the detector angles of Gammasphere an essentially spherical average over the gating transition was taken yielding an angular anisotropy (rather than an angular correlation) ratio.

It was not possible to extract intensities and angular ratios for all transitions shown in Fig. 1 from any single gate. However, the intensities of transitions and the angular-momentum assignments of states shown in Fig. 1 were confirmed from the analysis of spectra formed using several different gates. As an example of this analysis Table I gives the measured intensities, AC ratios ($R_{AC}$), angular anisotropy ratios ($R_{AA}$), and the angular-momentum assignments determined for transitions using a single gate on the 710 keV ($16^{(-)}\rightarrow 15^{(-)}$) transition in band *A*. The information contained in Table I is sufficient to show that the angular-momentum assignments of states in band *A* are firmly established.

Note, that the average $R_{AC}$ value for the dipoles in band *A* is $R_{AC}=0.80(2)$ and the average for the in-band stretched quadrupoles is $R_{AC}=1.34(6)$. These correlation ratios are consistent with an $E2/M1$ mixing ratio $\delta$ for the in-band stretched-dipole transitions of $\delta\approx 0.05$ (using the same phase convention as that used in Ref. [25])—see Fig. 6(b). This mixing ratio would correspond to a value of the angular anisotropy of $R_{AA}=0.86$ for a value of $\sigma/I=0.3$. The measured average of the dipoles in band *A* presented in Table I is

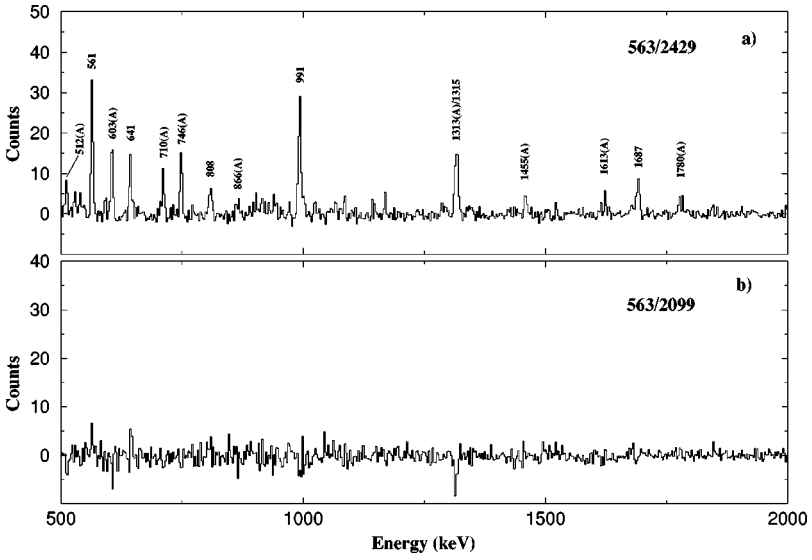


FIG. 5. (a) Spectrum obtained by requiring a double coincidence between the 563 keV transition of band *A* with the 2429 keV transition of band *B*. (b) Spectrum obtained by requiring a double coincidence between the 563 keV transition of band *A* with the 2099 keV transition of band *B*.

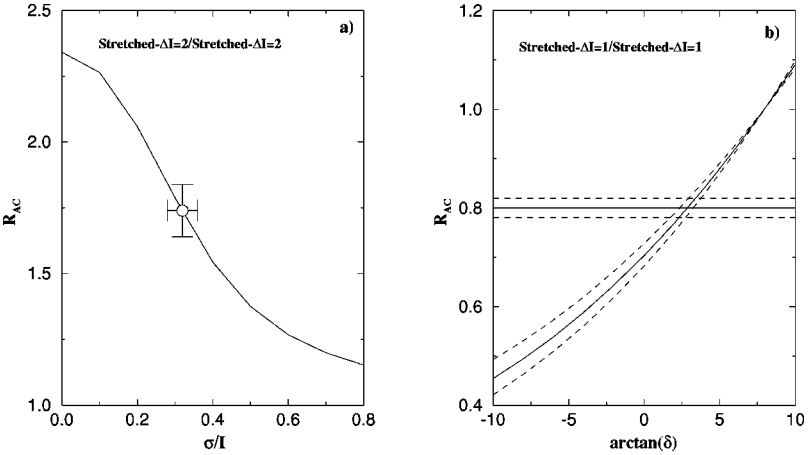


FIG. 6. (a) The solid curve is the calculated variation of $R_{AC}$ for a stretched-quadrupole ↔ stretched-quadrupole correlation as a function of the nuclear spin alignment parameter, $\sigma/I$ (see text). The open point is the experimental average value. The vertical errors indicate the experimental uncertainty of this quantity while the horizontal errors give the corresponding uncertainty in $\sigma/I$. (b) Plots of $R_{AC}$ for a stretched-dipole↔stretched-dipole correlation as a function of arctan ($\delta$) where $\delta$ is the $E2/M1$ mixing ratio. The horizontal solid line is the average experimental value for in-band $\Delta I=I$ transitions. The other solid curve is calculated assuming $\sigma/I=0.32$. Dashed lines and curves are the uncertainties.

$R_{AA}=0.79(2)$. Using the 710 keV dipole as a gate and assuming $\sigma/I=0.3$, a value of $R_{AA}\approx 1.41$ is expected for stretched quadrupole transitions. Assuming that all the low-lying stretched quadrupole transitions are electric quadrupoles, it follows that states in band *A* are likely negative parity.

As mentioned above, band *B* is much weaker than band *A*. Angular anisotropy measurements were sufficient to show the dipole character of the crossover transitions and the quadrupole character of the presumed *E*2 transitions. However, reliable $R_{AC}$ or $R_{AA}$ ratios could not be extracted for the transitions connecting band *B* to band *A*. Therefore, the angular-momentum assignments for the states in band *B* are unconfirmed. The intensity of band *A* is around ten times greater than the intensity of band *B* suggesting that band *A* is the yrast of the two structures in the region where they are fed. This suggests that the interband transitions may be $I \rightarrow I$ transitions as indicated in Fig. 1.

#### 3. $B(M1;I\rightarrow I\text{-}1)/B(E2;I\rightarrow I\text{-}2)$ ratios

The analysis described above shows that the $\Delta I=1$ crossover transitions in band *A* are relatively pure stretched dipoles, presumably magnetic dipoles as expected for decays between strongly coupled partner bands. It seems reasonable to assume that this is also the case for transitions in band *B*. The $B(M1;I\rightarrow I\text{-}1)/B(E2;I\rightarrow I\text{-}2)$ ratios can then be determined, which may help in assigning nucleon configurations to the bands. The expression used to determine these ratios is

$$\frac{B(M1;I\rightarrow I-1)}{B(E2;I\rightarrow I-2)} = 0.697\frac{E_\gamma(I\rightarrow I-2)^5}{E_\gamma(I\rightarrow I-1)^3}\frac{1}{\lambda} \times \frac{1}{(1+\delta^2)}[(\mu_N/eb)^2], \qquad (2)$$

where, $E_\gamma$ is given in MeV and $\lambda$ is the branching ratio expressed as

$$\lambda = \frac{I_\gamma(I\rightarrow I-2)}{I_\gamma(I\rightarrow I-1)}. \qquad (3)$$

The branching ratios were determined by setting a single gate on a transition decaying into the state of interest and measuring the intensities of the $\gamma$ rays depopulating that state. The small effect of the mixing ratio $\delta$ was ignored. The resulting $B(M1;I\rightarrow I\text{-}1)/B(E2;I\rightarrow I\text{-}2)$ ratios for bands *A* and *B* are given in Table II. The values for bands *A* and *B* agree within errors and are roughly constant for all measured values.

## III. THEORETICAL INTERPRETATION

### A. General considerations

The nucleus $^{64}$Zn has two protons and six neutrons outside the spherical doubly magic core of $^{56}$Ni ($N=Z=28$). Low-lying valence configurations involve active orbitals from the $\mathcal{N}=3$ $p_{3/2}$ and $f_{5/2}$ subshells and the $\mathcal{N}=4$ $g_{9/2}$ intruder subshell. Higher-angular-momentum states can be formed by exciting one or more protons from the $\mathcal{N}=3$ $f_{7/2}$ subshell across the $Z=28$ shell gap, giving rise to deformed, collective, band structures as observed in several nuclei of this mass region [1–13].

In an effort to assign configurations to the observed structures in $^{64}$Zn, configuration-dependent CNS calculations have been performed. The formalism described in Refs. [14,26] is followed. Pairing is neglected in these calculations so they can only be used to get a qualitative understanding of the states with low-angular momentum but they should become realistic for higher values, say $I>10\hbar$, in this mass region. Configurations will be labeled as $[p_1p_2,n_1n_2]$ defining the occupation of the active subshells,

$$\pi(f_{7/2})^{-p_1}(p_{3/2}f_{5/2})^{2+p_1-p_2}(g_{9/2})^{p_2}\nu(f_{7/2})^{-n_1}(p_{3/2}f_{5/2})^{6+n_1-n_2} \times (g_{9/2})^{n_2}.$$

That is, $p_1(n_1)$ is the number of proton (neutron) holes in the

TABLE I. Measured transition energies, intensities, angular correlation ratios ($R_{AC}$), angular anisotropy ratios ($R_{AA}$), and angular-momentum assignments for transitions in $^{64}$Zn measured from a single coincidence gate on the 710 keV stretched-dipole transition in band *A*. The intensities were corrected for detection efficiency and are given as a percentage of the 991 keV $2^+ \rightarrow 0^+$ transition. The numbers above the solid dividing line are in-band states of band *A* while those below it are from lower-lying states.

| $E_\gamma$ (keV) | Intensity | $R_{AC}$ | $R_{AA}$ | $I_i^\pi \rightarrow I_f^\pi$ |
|---|---|---|---|---|
| 508.1(5) | | | | $12^{(-)} \rightarrow 11^{(-)}$ |
| 512.0(5) | | | | $13^{(-)} \rightarrow 12^{(-)}$ |
| 563.3(3) | 65.5(3) | 0.78(2) | 0.76(2) | $14^{(-)} \rightarrow 13^{(-)}$ |
| 603.0(3) | 102.7(4) | 0.79(2) | 0.81(2) | $15^{(-)} \rightarrow 14^{(-)}$ |
| 709.5(3) | | | | $16^{(-)} \rightarrow 15^{(-)}$ |
| 746.4(3) | 87.2(4) | 0.86(2) | 0.81(3) | $17^{(-)} \rightarrow 16^{(-)}$ |
| 865.8(5) | 25.8(3) | 0.78(3) | 0.86(8) | $18^{(-)} \rightarrow 17^{(-)}$ |
| 914.5(5) | 29.6(3) | 0.80(5) | 0.83(5) | $19^{(-)} \rightarrow 18^{(-)}$ |
| 1082.1(5) | 13.7(3) | | | $20^{(-)} \rightarrow 19^{(-)}$ |
| 1142.0(5) | 4.1(8) | | | $21^{(-)} \rightarrow 20^{(-)}$ |
| 1395.6(9) | 4.2(2) | | | $22^{(-)} \rightarrow 21^{(-)}$ |
| 1292(1) | | | | $23^{(-)} \rightarrow 22^{(-)}$ |
| 1523(1) | | | | $24^{(-)} \rightarrow 23^{(-)}$ |
| 1020.0(5) | 6.0(2) | | | $13^{(-)} \rightarrow 11^{(-)}$ |
| 1074.7(5) | 15.9(4) | | | $14^{(-)} \rightarrow 12^{(-)}$ |
| 1166[a] | 52.4(4) | 1.27(11) | 1.25(6) | $15^{(-)} \rightarrow 13^{(-)}$ |
| 1312.5(9) | | | | $16^{(-)} \rightarrow 14^{(-)}$ |
| 1455.2(5) | | | | $17^{(-)} \rightarrow 15^{(-)}$ |
| 1613.3(6) | 57.4(11) | | 1.09(8) | $18^{(-)} \rightarrow 16^{(-)}$ |
| 1779.6(6) | 30.5(3) | 1.31(6) | 1.24(9) | $19^{(-)} \rightarrow 17^{(-)}$ |
| 1997.4(6) | 29.9(4) | 1.44(9) | 1.16(8) | $20^{(-)} \rightarrow 18^{(-)}$ |
| 2225.1(10) | 22.0(4) | 1.27(11) | 1.35(12) | $21^{(-)} \rightarrow 19^{(-)}$ |
| 2538.6(10) | 14.8(3) | 1.26(15) | 1.23(16) | $22^{(-)} \rightarrow 20^{(-)}$ |
| 2688.5(10) | 11.2(6) | 1.47(27) | 1.15(6) | $23^{(-)} \rightarrow 21^{(-)}$ |
| 2814(1) | 4.5(2) | | | $24^{(-)} \rightarrow 22^{(-)}$ |
| 3117(1) | 1.1(1) | | | $25^{(-)} \rightarrow 23^{(-)}$ |
| 3571(1) | | | | $26^{(-)} \rightarrow 24^{(-)}$ |
| 398.2(3) | 9.5(2) | 0.61(5) | 0.69(6) | $7^- \rightarrow 6^+$ |
| 429.8(3) | 1.2(1) | | 1.24(44) | $4^+ \rightarrow 4^+$ |
| 547.4(3) | 2.0(1) | | 0.87(15) | $8^{(-)} \rightarrow 7^{(-)}$ |
| 584.8(5) | 3.8(2) | | 0.80(8) | $12^{(-)} \rightarrow 11^{(-)}$ |
| 592.5(3) | 9.4(2) | 0.58(8) | 0.68(8) | $6^{(-)} \rightarrow 6^{(+)}$ |
| 617.9(5) | 1.7(1) | | | $5^- \rightarrow 4^{(+)}$ |
| 641.4(5) | 47.0(3) | 0.73(2) | 0.80(3) | $7^- \rightarrow 6^+$ |
| 656.7(5) | 3.0(1) | | 1.28(24) | $13^{(-)} \rightarrow 11^{(-)}$ |
| 771.2(5) | 2.9(1) | | 0.80(18) | $4^{(+)} \rightarrow 4^{+b}$ |
| 808.4(5) | 12.4(3) | | 0.71(6) | $2^+ \rightarrow 2^{+c}$ |
| 824.6(5) | 3.7(2) | | 1.66(13) | $7^{(-)} \rightarrow 5^{(-)}$ |
| 926.2(5) | 4.9(2) | | 1.43(11) | $5^- \rightarrow 3^-$ |
| 936.7(5) | 15.6(3) | 1.25(7) | 1.17(9) | $4^+ \rightarrow 2^+$ |
| 955.0(5) | 6.1(2) | 1.04(15) | 1.34(17) | $8^{(-)} \rightarrow 6^{(-)}$ |
| 971.1(5) | 5.3(2) | | 1.62(40) | $9^{(-)} \rightarrow 7^{(-)}$ |
| 991.0(5) | 100.0(19) | 1.19(3) | 1.17(2) | $2^+ \rightarrow 0^+$ |
| 999.9(6)[d] | 4.8(4) | | 0.92(3) | $6^{(+)} \rightarrow 4^{(+)}/4^{(+)} \rightarrow 4^+$ |
| 1029.9(5) | 3.3(2) | | 1.31(10) | $8^{(-)} \rightarrow 6^{(-)}$ |

TABLE I. (*Continued.*)

| $E_\gamma$ (keV) | Intensity | $R_{AC}$ | $R_{AA}$ | $I_i^\pi \rightarrow I_f^\pi$ |
|---|---|---|---|---|
| 1046.2(5) | 19.2(3) | 1.34(15) | 1.44(18) | $11^{(-)} \rightarrow 9^{(-)}$ |
| 1056.4(5) | 17.6(3) | 1.27(17) | 1.70(15) | $7^{(-)} \rightarrow 5^-$ |
| 1064.1(5) | 4.3(2) | | | $8^{(-)} \rightarrow 7^-$ |
| 1144.4(4) | 15.3(41) | 0.90(24) | 1.01(7) | $8^{(+)} \rightarrow 7^{(-)}$ |
| 1227.2(6) | 1.3(1) | | 1.39(9) | $7^{(-)} \rightarrow 5^-$ |
| 1260.3(7) | 15.6(2) | 1.21(12) | 1.15(11) | $11^{(-)} \rightarrow 9^{(-)}$ |
| 1304.9(5) | 5.8(2) | | | $12^{(-)} \rightarrow 11^{(-)}$ |
| 1315[e] | 113.4(5) | 1.12(4) | 1.39(3) | $4^+ \rightarrow 2^+ / 9^{(-)} \rightarrow 7^-$ |
| 1340.0(7) | 12.4(2) | 1.26(15) | 1.26(11) | $6^{(+)} \rightarrow 4^+$ |
| 1363.0(4) | 6.9(2) | 1.46(32) | 1.33(31) | $10^{(-)} \rightarrow 8^{(-)}$ |
| 1397.0(5) | 4.3(2) | | | $8^{(+)} \rightarrow 7^-$ |
| 1500.3(5) | 9.2(2) | 1.74(20) | 1.64(24) | $6^+ \rightarrow 4^+$ |
| 1618.6(5) | 20.4(5) | | | $5^- \rightarrow 4^+$ |
| 1622.5(8) | 0.8(5) | | | $11^{(-)} \rightarrow 10^{(-)}$ |
| 1686.9(5) | 45.5(4) | 1.27(17) | 1.36(5) | $6^+ \rightarrow 4^+$ |
| 1773.2(10) | 2.8(5) | | | $6^{(+)} \rightarrow 4^+$ |
| 1799.6(7) | 5.5(2) | | 1.56(33) | $2^+ \rightarrow 0^+$ |
| 1850.4(10) | 2.3(4) | | | $5^{(-)} \rightarrow 4^+$ |
| 1935.3(7) | 4.1(3) | 1.61(28) | 1.46(10) | $6^+ \rightarrow 4^+$ |
| 2005.0(10) | 2.4(3) | | | $3^- \rightarrow 2^+$ |
| 2037.8(7) | 5.8(3) | 1.66(22) | 1.37(18) | $8^{(+)} \rightarrow 6^+$ |
| 2086.2(7) | 5.6(2) | | 1.12(43) | $4^{(+)} \rightarrow 2^+$ |
| 2129.7(7) | 2.6(2) | | 1.49(9) | $8^{(+)} \rightarrow 6^+$ |
| 2158.3(9) | 4.3(2) | | | $13^{(-)} \rightarrow 12^{(-)}$ |
| 2321.9(9) | 3.6(2) | | | $11^{(-)} \rightarrow 10^{(+)}$ |
| 2720(1) | 1.1(1) | | | $14^{(-)} \rightarrow 12^{(-)}$ |
| 2886(1) | 1.1(1) | | 1.52(30) | $12^{(-)} \rightarrow 10^{(-)}$ |
| 2950(1) | 4.4(2) | 0.87(8) | 0.91(8) | $12^{(-)} \rightarrow 11^{(-)}$ |
| 3247(1) | 2.9(1) | | 1.24(10) | $13^{(-)} \rightarrow 11^{(-)}$ |
| 3461(1) | 5.5(2) | 1.37(29) | 1.69(51) | $13^{(-)} \rightarrow 11^{(-)}$ |

[a]contaminated.
[b]$R_{AA}$ is low for this assignment.
[c]$R_{AA}$ is low for this assignment.
[d]multiple unresolved transitions.
[e]multiple unresolved transitions.

$f_{7/2}$ subshell and $p_2(n_2)$ is the number of protons (neutrons) in the $g_{9/2}$ subshell. Similar calculations have previously been carried out for $^{64}$Zn [2] and for several other nuclei in this region, including $^{59}$Cu [11], $^{62}$Zn [1,3], and $^{68}$Ge [9]. In general, for a nucleus with only a few particles (and holes) outside the $Z=N=28$ core, the configurations are rather pure and easy to interpret. With more particles outside the core, as in the case of $^{68}$Ge [9], the situation becomes more complex.

It is useful at this stage to make a few remarks on terminology and to broadly outline the main points in the sections to come. The word configuration is used to refer to the occupation of active subshells as discussed in the preceding paragraph. As shall be seen in Sec. III B, standard CNS calculations do not take into account the specific distribution of the nucleons within that configuration. In other words, different states can be formed by the redistribution of nucleons within specific subshells belonging to the same "fixed" configuration. In order to trace these states, it is necessary to go beyond the standard CNS formalism. The extended CNS calculations, and the resulting interpretation of band *A*, are presented in Sec. III C. Possible interpretations of band *B* are discussed in Sec. III D.

### B. Standard CNS calculations

First, it is worthwhile to give a general overview of the calculated structures in $^{64}$Zn. Using standard parameters [26], the yrast states and other low-lying configurations for different combinations of parity and signature were investigated. These states are shown relative to a standard rotating reference [14] in Fig. 7. The highest angular momentum

TABLE II. Measured $B(M1;I\rightarrow I\text{-}1)/B(E2;I\rightarrow I\text{-}2)$ ratios for bands $A$ and $B$ (above and below the solid dividing line, respectively).

| $E_\gamma(\Delta I=1)$ | $E_\gamma(\Delta I=2)$ | $B(M1;I\rightarrow I\text{-}1)/B(E2;I\rightarrow I\text{-}2)(\mu_N/e\text{b})^2$ |
|---|---|---|
| 563 | 1075 | 15.3(10) |
| 603 | 1166 | 12.8(9) |
| 710 | 1313 | |
| 746 | 1455 | 12.3(18) |
| 866 | 1613 | 10.6(5) |
| 915 | 1780 | 12.6(11) |
| 1082 | 1997 | 15.3(10) |
| 1142 | 2225 | 14.5(12) |
| 1396 | 2539 | 15.2(12) |
| 1292 | 2689 | 12.7(18) |
| 856 | 1860 | 9.9(21) |
| 1067 | 1924 | 12.1(20) |
| 1032 | 2099 | 14.0(40) |

which can be built in the valence space of $(p_{3/2}f_{5/2})$ protons and neutrons is $I=10$. However, this $10^+$ state is calculated to have a relatively high excitation energy. The lowest calculated states for $I=10-15$ involve one, two, or even three $g_{9/2}$ particles. These configurations often terminate in low-lying noncollective aligned states at a large oblate deformation. At higher angular momentum, it becomes favorable to promote one proton from the $f_{7/2}$ subshell across the $Z=28$ gap. These configurations are drawn with thick shaded lines in Fig. 7. For even higher values of the angular momentum, it becomes favorable to create more holes (particles) in the $f_{7/2}(g_{9/2})$ subshells leading to larger deformations and enhanced collectivity.

The contribution to the total angular momentum from the different subshells is given for low-lying aligned states in Table III. The information in this table also allows the signature of the different groups of orbitals to be read out. For those configurations which are strongly downsloping in Fig. 7, it generally appears that the $(p_{3/2}f_{5/2})$ neutrons do not contribute their maximum angular momentum to the terminating state. This occurs for the [01,01] $13^+$ and $14^+$ states, for the [11,01] $18^+$ and $19^+$ states, and for the [00,01] $11^-$ state in which the five $(p_{3/2}f_{5/2})$ $\alpha=1/2$ neutrons couple to $I=2.5$. The states for which the $(p_{3/2}f_{5/2})$ neutrons couple to $I=4.5$ or $I=6.5$ are less favored in energy and, therefore, they are not drawn in Fig. 7 (with the exception of the $13^-$ state which belongs to the same configuration as the [00,01] $11^-$ state). If the five $(p_{3/2}f_{5/2})$ neutrons have $\alpha=-1/2$, the states are calculated to be less favored energetically but they continue smoothly to the state where these five neutrons couple to their maximum angular momentum of $I=5.5$. This occurs for the [11,01] configuration terminating at $21^+$ and $22^+$, and for the [00,01] configuration terminating at $14^-$. For configurations with four $(p_{3/2}f_{5/2})$ neutrons, there is a competition between terminating states involving either the full angular-momentum contribution from these neutrons of $I=6$ or if they only contribute $I=4$. When $\alpha=1$, it is the configuration in which these neutrons contribute $I=3$, which becomes competitive in energy while the states requiring the maximum contribution of $I=5$ appear to be much less favored. Examples of these $\nu(p_{3/2}f_{5/2})^4$ couplings are seen in Table III and will be discussed in more detail below for the [11,02] configuration.

To compare experiment with calculation, band $A$ is of main interest since band $B$ does not have firm $I^\pi$ assignments. Band $A$ was assigned to the [11,02] configuration in Ref. [2]. The analysis of Ref. [2] shows that this configuration assignment is consistent with the measured small positive $E2/M1$ mixing ratios and the deduced $B(M1;I\rightarrow I-1)/B(E2;I\rightarrow I-2)$ values. Now that band $A$ has been connected to the low-angular-momentum states and observed to the $I^\pi=26^{(-)}$ state (see Fig. 1), this assignment has additional support. There are two calculated [11,02] configurations which are relatively low in energy (see Fig. 7). These two configurations differ in the distribution of the four neutrons

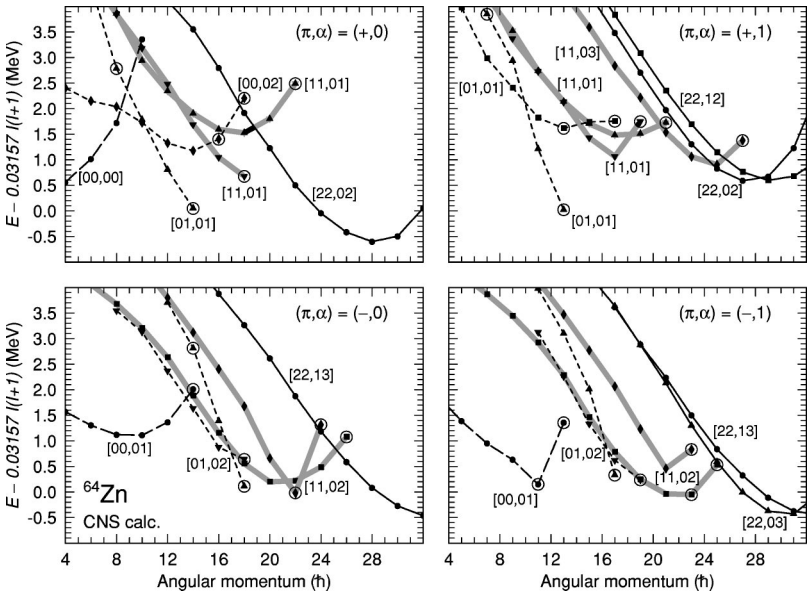


FIG. 7. The calculated low-lying rotational bands of $^{64}$Zn drawn relative to a rigid-rotor reference. Each panel corresponds to fixed parity $\pi$ and signature exponent $\alpha$. The configurations with one proton hole in the $f_{7/2}$ subshell are drawn with thick shaded lines. Aligned states at, or very close to, $\gamma=60°$ are circled.

TABLE III. Low-lying calculated terminating states in $^{64}$Zn. The $(\varepsilon_2,\varepsilon_4)$ deformation at termination ($\gamma=60°$) is given in the third column. The angular-momentum contribution from different groups of orbitals $[(pf)\equiv(p_{3/2}f_{5/2})]$ is shown as a subscript in the fourth column.

| $I$ | $[p_1p_2,n_1n_2]$ | Deformation, $(\varepsilon_2,\varepsilon_4)$ | Configuration |
|---|---|---|---|
| $13^+$ | [01,01] | (0.24,−0.014) | $\pi(pf)^1_{1.5,2.5}\,(g_{9/2})^1_{4.5}$ |
| $14^+$ | | (0.26,−0.018) | $\nu(pf)^5_{2.5}\,(g_{9/2})^1_{4.5}$ |
| $18^+$ | [11,01] | (0.24,−0.014) | $\pi(f_{7/2})^{-1}_{2.5,3.5}\,(pf)^2_4\,(g_{9/2})^1_{4.5}$ |
| $19^+$ | | (0.23,−0.009) | $\nu(pf)^5_{2.5}\,(g_{9/2})^1_{4.5}$ |
| $21^+$ | [11,01] | (0.23,−0.023) | $\pi(f_{7/2})^{-1}_{2.5,3.5}\,(pf)^2_4\,(g_{9/2})^1_{4.5}$ |
| $22^+$ | | (0.20,−0.010) | $\nu(pf)^5_{5.5}\,(g_{9/2})^1_{4.5}$ |
| $11^-$ | [00,01] | (0.18,0.005) | $\pi(pf)^2_4$ |
| $14^-$ | | (0.18,−0.007) | $\nu(pf)^5_{2.5,5.5}\,(g_{9/2})^1_{4.5}$ |
| $17^-$ | | (0.26,0.005) | |
| $18^-$ | [01,02] | (0.28,0.000) | $\pi(pf)^1_{1.5,2.5}\,(g_{9/2})^1_{4.5}$ |
| $18^-$ | | (0.27,−0.008) | $\nu(pf)^4_{3,4}\,(g_{9/2})^2_8$ |
| $19^-$ | | (0.30,−0.015) | |
| $23^-$ | | (0.28,−0.013) | |
| $25^-$ | [11,02] | (0.25,−0.004) | $\pi(f_{7/2})^{-1}_{2.5,3.5}\,(pf)^2_4\,(g_{9/2})^1_{4.5}$ |
| $26^-$ | | (0.22,0.010) | $\nu(pf)^4_{4,6}\,(g_{9/2})^2_8$ |
| $22^-$ | [11,02] | (0.27,−0.002) | $\pi(f_{7/2})^{-1}_{2.5,3.5}\,(pf)^2_4\,(g_{9/2})^1_{4.5}$ |
| $23^-$ | | (0.25,0.010) | $\nu(pf)^4_3\,(g_{9/2})^2_8$ |

in the $(p_{3/2}f_{5/2})$ orbitals. The configuration which is lowest for most angular-momentum values has two neutrons in each of the $\alpha=\pm1/2$ orbitals, while the other configuration has three neutrons in $\alpha=1/2$ and one in $\alpha=-1/2$. For the terminating states of this latter configuration (listed in Table III, $I=22,23$) these four $(p_{3/2}f_{5/2})$ neutrons couple to $I=3$. However, the corresponding band is calculated to be very irregular and lie low in energy for only a few angular-momentum values, especially $I=22$. Therefore, it is only the more regular [11,02] band which is relevant for the interpretation of band *A*.

The calculated $\alpha=1$ states (odd-$I$ values) behave regularly only up to $I^\pi=23^-$ which is predicted to be a noncollective state with $\gamma=60°$. This aligned $23^-$ state terminates the lowest [11,02] band. The aligned $25^-$ state, connected to this $23^-$ state in Fig. 7, corresponds to the terminating state of a different excited sequence. As seen in Table III, the difference between these two aligned states is that the four neutrons in the $(p_{3/2}f_{5/2})$ orbitals contribute either $4\hbar$ or $6\hbar$ of angular momentum, respectively. The calculated termination at $I^\pi=23^-$ disagrees with the observed odd-$I$ sequence which behaves regularly all the way up to and including the $I^\pi=25^-$ state. In contrast, the $\alpha=0$ states (even-$I$ values) behave regularly all the way up to the $I^\pi=26^-$ state in agreement with experiment. It is surprising that the calculated odd-$I$ and even-$I$ states display this different behavior as they approach termination since they only differ by the signature of the $f_{7/2}$ hole (see Table III). It is probable that this discrepancy can be removed by making small changes to the single-particle parameters used in the calculation (see below).

The shape trajectories for the two lowest [11,02] configurations are shown in Fig. 8. Consider first the yrast, odd-angular-momentum states for which the shape changes smoothly from $\varepsilon_2\approx0.31$, $\gamma\approx20°$ at $I^\pi=11^-$ to the terminating $I^\pi=23^-$ state at $\varepsilon_2\approx0.28$, $\gamma=60°$. This contrasts with the shape trajectory for the even-$I$ states which follows the odd-$I$ trajectory up to $I\approx20$ but then moves toward decreasing $\varepsilon_2$ values (with approximately a constant value of $\gamma$) before reaching a noncollective $\gamma=60°$ $I^\pi=26^-$ state. The deformation of this $I=26$ state is considerably smaller ($\varepsilon_2=0.22$) than

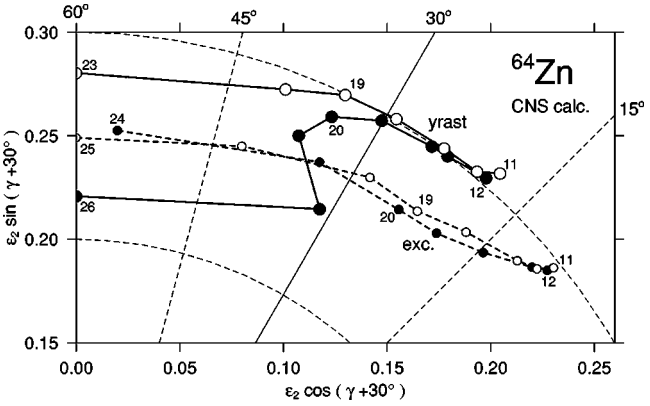


FIG. 8. Calculated deformations for the [11,02] configurations in $^{64}$Zn using standard parameters [26]. The yrast states are shown by large circles and full lines, while the states with one excited $\alpha=-1/2$ low-$j$, $\mathcal{N}=3$ neutron by smaller circles and dashed lines. The open (closed) circles are for odd-$I$ (even-$I$) states.

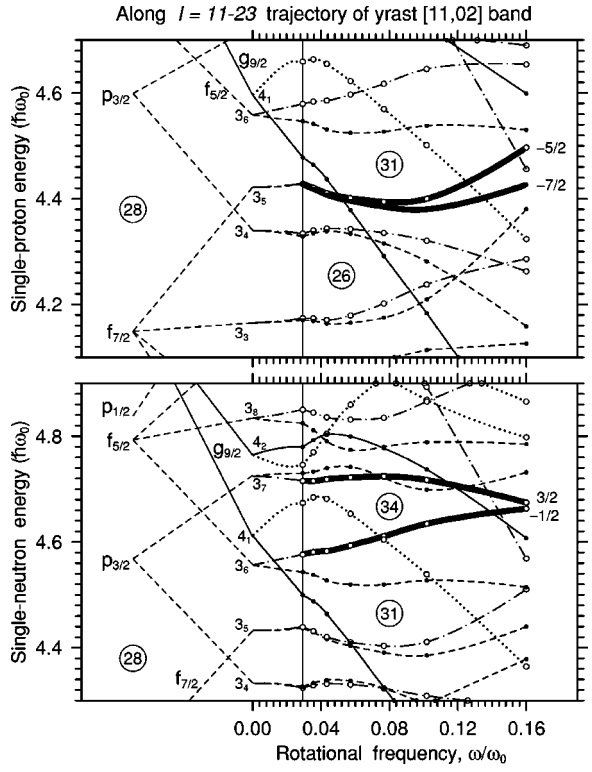


FIG. 9. Single-particle orbitals along the path, calculated with standard parameters as in Fig. 8, of the lowest $I=11-23$ states in the [11,02] configuration of $^{64}$Zn. The spherical origin of the orbitals is traced schematically, first by varying the deformation and then by adding a cranking frequency, $\omega$. At $\omega=0$, the orbitals are labeled by their oscillator shell, $\mathcal{N}$, and by the position in that $\mathcal{N}$ shell as a subscript. Positive-parity states are shown by full or dotted lines while negative-parity states have dashed or dot-dashed lines. Symbols (circles for $\alpha=-1/2$ and dots for $\alpha=+1/2$) are drawn at the frequencies corresponding to the $I=11,13,\ldots,23$ states while the deformation at these angular momentum values can be read out in Fig. 8. The frequency of the terminating $I=23$ state is not well defined and was chosen to give smooth curves for the single-particle energies. The orbitals which are either occupied or empty in the [11,02] bands assigned to the observed band *A* are drawn by thick shaded lines. For these orbitals, the aligned angular momentum along the symmetry axis at termination ($\gamma=60°$) is given on the right-hand side.

that of the $I=23$ state ($\varepsilon_2=0.28$). The *S* shape of the even-*I* trajectory suggests some kind of band-crossing at $I\approx 22\hbar$.

The single-particle orbitals along the odd-*I* shape trajectory are drawn in Fig. 9 where, at each deformation, the rotational frequency has been fitted to give the appropriate angular-momentum value. For the protons, there is a big gap at $Z=31$ and the odd-*I* states are formed by creating one hole in the highest $f_{7/2}$ orbital (labeled $3_5$) below this gap, while the even-*I* states require the hole to be in the signature-partner orbital. These orbitals, which are drawn with thick shaded lines in Fig. 9, are essentially degenerate at low-angular-momentum but separate in energy at higher angular-momentum. The neutron orbitals are filled up to the $N=34$ gap. At $\gamma=60°$ there is an orbital just below the gap, labeled $3_6$, which has an aligned angular momentum of $m_i=-0.5\hbar$. At this same point in the shape trajectory, there is another orbital at slightly higher energy, labeled $3_7$, which has the same signature and parity but an aligned angular momentum of $m_i=1.5$. These differences in the $m_i$ values imply that if the 34th particle is raised to the higher-lying $3_7$ orbital, an excited configuration exists which will terminate $2\hbar$ higher than the yrast sequence. That is, the excited configuration will terminate at $I=25$. The even-*I* states appear to behave differently, terminating at $I^\pi=26^-$ and not at $I^\pi=24^-$. This suggests that, for the corresponding shape trajectory, the ordering of these two neutron orbitals ($3_6$ and $3_7$) is already reversed at $\gamma=60°$. Therefore, they must interact before reaching the noncollective limit at $\gamma=60°$, which is consistent with the band-crossing scenario discussed above. The two configurations which interact will have the same labeling within the standard scheme. In order to study such a situation in detail the CNS formalism must be extended to include a way to follow such structures which may be regarded as excitations within a "fixed" configuration.

### C. Extended CNS calculations

In principle, it should be straightforward to calculate not only the yrast states but also excited states associated with fixed configurations. However, without additional constraints, the first excited state might correspond to a different excitation at each angular-momentum value. To overcome this problem it is possible to define in which group of orbitals an excitation is allowed (for example, in the low-*j* $\mathcal{N}=3$ orbitals with $\alpha=-1/2$). The difficulty is then to define the excited state in the full space of deformation and rotational frequency. In general, this is not possible because of different virtual crossings between orbitals with identical quantum numbers. For example, an excited state could correspond to either a single-particle excitation at a constant deformation or to a state in a secondary minimum at a different deformation. However, by limiting the changes in deformation and rotational frequency, it is often possible to define a unique yrast sequence and to specify which excitation is allowed with respect to these yrast states. In order to provide a full interpretation of band *A* and to search for possible explanations of band *B*, the CNS formalism as described in Ref. [14] was generalized to calculate and identify excitations of this kind.

Considering the orbitals in Fig. 9, the lowest states of the [11,02] type are well defined. Starting from these states, the next highest excited states have been calculated, specifying excitations within the low-*j*, $\mathcal{N}=3$, $\alpha=-1/2$ neutron orbitals. This corresponds to a neutron being excited from the lower ($3_6$) to the upper ($3_7$) thick shaded orbital in the lower panel of Fig. 9. For odd-*I* excited states, a smooth, well-defined deformation trajectory is obtained, which can be followed up to $I^\pi=25^-$ (see Fig. 8). This state is noncollective with $\varepsilon_2\approx 0.25$, $\gamma=60°$ and was connected smoothly to the aligned yrast $I^\pi=23^-$ state in Fig. 7. For the even-*I* states, the yrast band can be followed to the $I^\pi=26^-$ state as discussed above.

There seems to be a clear tendency for the highest-angular-momentum states to be calculated at a higher excitation energy relative to the observed energies. For $^{64}$Zn with

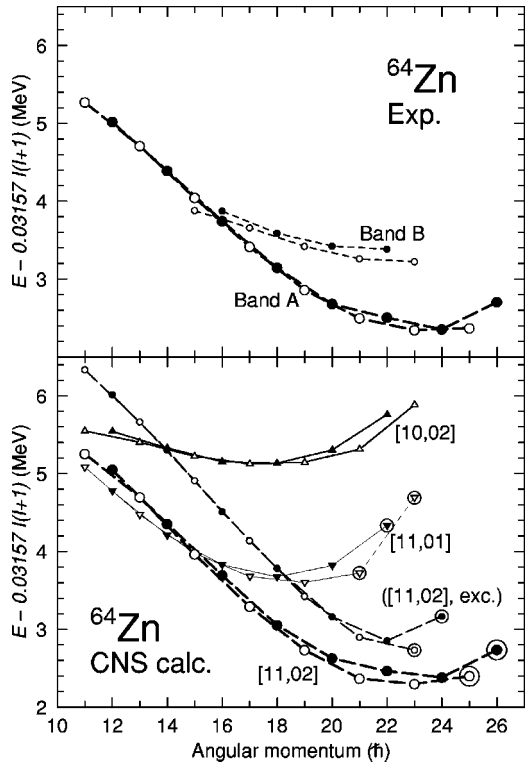


FIG. 10. Comparison between the observed bands *A* and *B* (upper panel) and the calculated configuration (using revised parameters—see text) assigned to band *A* and possible configurations which could be assigned to band *B*. Full (long-dashed) lines indicate positive (negative) parity while short-dashed lines are drawn when the parity is not known. The open (closed) symbols are for odd-*I* (even-*I*) states. Experiment and theory have been normalized in the high-spin range of band *A* contrary to the more standard convention to normalize for the ground state. Aligned states at, or very close to, $\gamma=60°$ are circled. Calculated energies of the [11,01] configuration are given only for the collective minima where energy and deformation varies smoothly with angular momentum *I*.

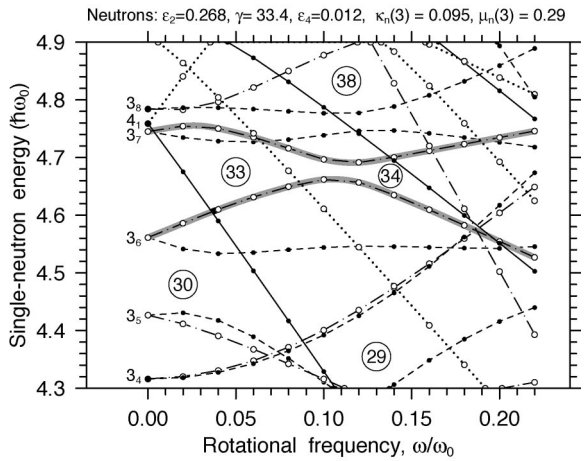


FIG. 11. Neutron orbitals at a deformation close to that calculated for the yrast [11,02] configurations of $^{64}$Zn at $I=21,22$. Positive-parity states are shown by full or dotted lines while negative-parity states have dashed or dot-dashed lines. Open circles indicate $\alpha=-1/2$ and dots indicate $\alpha=+1/2$. The parameters fitted to describe the positive parity states in $^{59}$Cu are used [27]. The two orbitals which pass through a virtual crossing at $\omega\approx 0.12\omega_0$ are drawn with thick shaded lines.

only a few particles in the $(p_{3/2}f_{5/2})$ subshells, the highest-angular-momentum states will become more favored if the high-*j* subshells are made to have lower energy in the calculation (that is, the $f_{5/2}$ subshell is lowered relative to the $p_{3/2}$ subshell). The parameters recently used to describe the decay out of the superdeformed band in $^{59}$Cu [27] indicate that such small changes are reasonable. In that case, the $f_{5/2}$ subshell was found to be approximately 300 keV closer to the $p_{3/2}$ subshell (corresponding to $0.025\hbar\omega_0$ closer in oscillator units as used in Fig. 9). New calculations for the configurations in $^{64}$Zn have been performed using these revised parameters. The new calculations for the yrast [11,02] sequences are compared with band *A* in Fig. 10. The agreement with experiment is almost perfect all the way from the lowest $I^\pi=11^-,12^-$ states to the terminating $I^\pi=25^-,26^-$ states. The calculated shape trajectory for the even-*I* states is very similar to that already shown in Fig. 8. The odd-*I* states now follow a trajectory close to that of the even-*I* states with a similar *S* shape and terminating at $\varepsilon_2\approx 0.25$, $\gamma=60°$.

Shown in Fig. 11 are the calculated single-neutron orbitals using the revised parameters. The calculation was performed at a fixed deformation close to the predicted shape associated with the yrast and excited [11,02] bands at $I=21,22$. It is evident that the sixth and seventh $\alpha=-1/2$, $\mathcal{N}=3$ orbitals come close to each other, interchanging character at $\omega=0.12\omega_0$, and passing through a virtual crossing. This is the approximate frequency at which the $I=21,22$ states are expected. This crossing is not clearly visible in the behavior of calculated energies drawn in Fig. 10, indicating a large interaction strength. However, this interaction will influence the curvature of the calculated sequences in Fig. 10 and, since there is excellent agreement with experiment, this crossing is important for a detailed understanding of band *A*.

### D. Possible interpretations of band *B*

It is interesting to see if an interpretation can be found for band *B*, assuming that the suggested angular-momentum assignments in Fig. 1 are correct. The $B(M1;I\rightarrow I\text{-}1)/B(E2;I\rightarrow I\text{-}2)$ ratios measured for bands *A* and *B* are identical within errors (see Table II) supporting the suggestion that the two bands are based on similar configurations involving only one $f_{7/2}$ proton hole. This is also consistent with the range of angular momentum over which the band is seen.

There are several possible interpretations of band *B*. The band might correspond to the second [11,02] configuration (drawn in Fig. 7) which terminates in aligned states with $I^\pi=22^-$ and $I^\pi=23^-$, which is consistent with the suggested angular-momentum assignments. However, the calculation for this configuration fails to reproduce several features of the observed band *B* including its excitation energy relative to band *A*. It is not drawn in the lower panel of Fig. 10.

Another possibility is that band *B* could be an excitation of the yrast [11,02] configuration as discussed in the preceding section. The band resulting from such a calculation ter-

minates at $I^{\pi}=23^{-}$ and $I=24^{-}$. The prediction for the two signatures is drawn in the lower panel of Fig. 10. The calculated energies at the highest angular momenta are in general agreement with experiment but the discrepancy gets worse for lower $I$ values.

As drawn in Fig. 1, band $A$ is clearly yrast when compared with band $B$ at high angular momentum (which is also reasonable from the point of view of the relative population of the two bands) but the energy difference between the two bands decreases with decreasing angular momentum. It would then seem reasonable to expect that the underlying configuration of band $B$ involves fewer $g_{9/2}$ particles. Possible configurations of this kind are [11,01] (with one $g_{9/2}$ proton and one $g_{9/2}$ neutron) or [10,02] (no $g_{9/2}$ protons and two $g_{9/2}$ neutrons). The calculated sequences based on these configurations are drawn in the lower panel of Fig. 10.

The [11,01] sequences are also drawn in Fig. 7, where standard parameters are used. Independent of the parameters used, there is a total four bands: $f_{7/2}$ signature partners are formed with the $(p_{3/2}f_{5/2})$ neutrons having either $\alpha=1/2$ or $\alpha=-1/2$. While the $\alpha=1/2$ bands are lower in energy for some angular-momentum values, it is the $\alpha=-1/2$ bands, with the $(p_{3/2}f_{5/2})$ neutrons coupled to a maximum spin of $5.5\hbar$ (see Table III), which behave smoothly and which are therefore most naturally associated with band $B$. Indeed, as seen in Fig. 10, the general characteristics of these calculated sequences agree much better with band $B$ (using the suggested angular-momentum assignments) than the other configurations drawn in the figure. However, the observed band continues to a suggested angular momentum of $I=23\hbar$, while the maximum angular momentum for the calculated configuration is $22\hbar$. One possibility would be that the state labeled as $I=(23)$ in band $B$ belongs to a different configuration. It should be noted that an $I=23$ state can be formed in the [11,01] configuration when the five $(p_{3/2}f_{5/2})$ neutrons have $\alpha=1/2$, in which case they can couple to $I=6.5\hbar$. Although this $23^{-}$ state is at a fairly high energy, it is drawn in Fig. 7 and connected to the $23^{-}$ state with a short-dashed line.

The [10,02] configuration appears to be too high in excitation energy to be a reasonable alternative (see Fig. 10). The high excitation energy is due to the large signature splitting between the two lowest $g_{9/2}$ neutron levels, which makes it energetically unfavorable to have two neutrons occupying these orbitals.

## IV. SUMMARY

In summary, high-angular-momentum states in $^{64}$Zn were investigated in an experiment using Gammasphere and the Microball. The level scheme was considerably revised and extended. The main focus of this paper has been on two strongly coupled bands. One of these bands was known from a previous study. This structure has been firmly linked to low-lying states, establishing the excitation energies, angular momenta, and probable parity of the in-band states. An excited band is seen to decay to the lower-lying band and several interband transitions have been identified. The angular momenta and parity of the states in this second band could not be firmly established. These structures are important examples of the onset of collective rotational behavior in the limited valence space outside the $N=Z=28$ spherical shell gaps.

In order to interpret the bands, the standard cranked-Nilsson-Strutinsky formalism was extended to allow yrast and excited states to be calculated within fixed configurations and to find their self-consistent deformations. The lowest collective band in $^{64}$Zn is interpreted as based on the $\pi(f_{7/2})^{-1}(p_{3/2}f_{5/2})^{2}(g_{9/2})^{1}\nu(p_{3/2}f_{5/2})^{4}(g_{9/2})^{2}$ configuration (labeled [11,02] in our notation) and the calculations reproduce the observed in-band states to an excellent accuracy. The second band has several alternative interpretations, but on the basis of the current work it is impossible to distinguish between them. One aspect that may provide an important clue is the interband decay from this excited structure to the lower band.

## ACKNOWLEDGMENTS

We would like to express our gratitude to the operations staff of ATLAS and to John Greene (ANL) for making the target foils. This work was supported in part by the U.S. DoE under Contract Nos. DE-AC03-76SF00098 (LBNL), W-31-109-ENG-38 (ANL), and DE-FG05-88ER40406 (WU), the Swedish Science Research Council and the Natural Sciences and Engineering Research Council of Canada.

[1] C. E. Svensson *et al.*, Phys. Rev. Lett. **79**, 1233 (1997).
[2] A. Galindo-Uribarri *et al.*, Phys. Lett. B **422**, 45 (1998).
[3] C. E. Svensson *et al.*, Phys. Rev. Lett. **80**, 2558 (1998).
[4] D. Rudolph *et al.*, Phys. Rev. Lett. **80**, 3018 (1998).
[5] C. E. Svensson *et al.*, Phys. Rev. Lett. **82**, 3400 (1999).
[6] D. Rudolph *et al.*, Phys. Rev. Lett. **82**, 3763 (1999).
[7] C. H. Yu *et al.*, Phys. Rev. C **60**, 031305(R) (1999).
[8] C. H. Yu *et al.*, Phys. Rev. C **62**, 041301 (2000).
[9] D. Ward *et al.*, Phys. Rev. C **63**, 014301 (2000).
[10] C. Andreoiu *et al.*, Phys. Rev. C **62**, 051301(R) (2000).
[11] C. Andreoiu *et al.*, Eur. Phys. J **14**, 317 (2002).
[12] D. Rudolph *et al.*, Phys. Rev. Lett. **86**, 1450 (2001).
[13] W. Reviol *et al.*, Phys. Rev. C **65**, 034309 (2002).
[14] A. V. Afanasjev, D. B. Fossan, G. J. Lane, and I. Ragnarsson, Phys. Rep. **322**, 1 (1999).
[15] I. Y. Lee, Nucl. Phys. **A520**, 641c (1990).
[16] D. G. Sarantites *et al.*, Nucl. Instrum. Methods Phys. Res. A **381**, 418 (1996).
[17] M. Devlin *et al.*, Nucl. Instrum. Methods Phys. Res. A **383**, 506 (1996).
[18] C. E. Svensson *et al.*, Nucl. Instrum. Methods Phys. Res. A **396**, 228 (1997).
[19] D. C. Radford, Nucl. Instrum. Methods Phys. Res. A **361**, 297 (1995).

[20] D. Seweryniak *et al.*, Nucl. Instrum. Methods Phys. Res. A **340**, 353 (1994).
[21] D. N. Simister *et al.*, J. Phys. G **6**, 81 (1980).
[22] J. Jabbour *et al.*, Nucl. Phys. **A464**, 260 (1987).
[23] B. Crowell *et al.*, Phys. Rev. C **50**, 1321 (1994).
[24] K. Furutaka *et al.*, Z. Phys. A **358**, 279 (1997).
[25] T. Yamazaki, At. Data Nucl. Data Tables **A3**, 1 (1967).
[26] T. Bengtsson and I. Ragnarsson, Nucl. Phys. **A436**, 14 (1985).
[27] C. Andreoiu *et al.*, Phys. Rev. Lett. **91**, 232502 (2003).